WEST-EAST HIGH SPEED FLOW FIELD CONFERENCE
19-22, November 2007
Moscow, Russia

CABARET SCHEME FOR NON-LINEAR AEROACOUSTIC PROBLEMS

Sergey A. Karabasov*, Vasily M. Goloviznin****

** Whittle Laboratory*
Department of Engineering University of Cambridge
1, JJ Thompson Avenue, Cambridge CB3 0D
Email:sak36@eng.cam.ac.uk
***Moscow Institute of Nuclear Safety (IBRAE)*
52, B.Tulskaya Street
Moscow, 115191, Russia
Email:gol@ibrae.ac.ru

Key words: Computational fluid dynamics, aeroacoustics, simulation of high-speed flows, high-resolution numerical methods, shock-capturing, low-dispersive and low-dissipative numerical schemes

Abstract. This paper is devoted to a new efficient numerical method for aeroacoustic applications. The method is second-order accurate, and has a very compact numerical stencil. It combines merits of shock-capturing and low-dispersion and low-dissipation approaches on coarse grids. Numerical examples are provided for several model problems on structured orthogonal and curvilinear Cartesian grids.

1. INTRODUCTION

Efficient numerical schemes are highly demanded for simulations of unsteady flows with a wide disparity of frequencies and length scales. In particular, the problems when multiple scales emerge are common for aeroacoustics [0]. There are many successful numerical techniques used in computations of unsteady non-linear flows at present but there are only a few which are designed to emphasise more than one particular property of the governing equations. For instance, in compressible flow simulations higher-order optimised finite-difference schemes use a quasi-linear form, as opposed to a conservation form, of the equations to mimic the Fourier wave properties such as linear wave dispersion and non-dissipation. On the other hand, in higher order shock-capturing schemes it is the conservation form, which is laid in the basis and high-order reconstruction and interpolation procedures, are used to improve the linear properties of the basic method. Traditional second-order shock capturing schemes are known to be too dissipative for linear wave computations on standard engineering numerical grids. This paper is devoted to a novel low-dispersion and low-dissipation method with shock-capturing capabilities, which has much better linear wave properties, and which uses a non-linear correction procedure to enforce the maximum principle without smearing the linear flow field.

1.1. Basic scheme

To illustrate ideas on a simple example, a one-dimensional scalar advection equation is considered

$$\frac{\partial \varphi}{\partial t} + \frac{\partial \varphi}{\partial x} = 0$$

on a finite-difference grid which is non-uniform in space $x_{i+1} - x_i = h_{i+1/2}$ and time $t^{n+1} - t^n = \tau^{n+1/2}$.

The equation is approximated by introducing dual variables referred to the same scalar quantity φ, and staggered in space. A "conservative-type" variable $\psi^n_{i+1/2}$ is defined in cell centres, and an "advection-type" one φ^n_i is defined at cell boundaries.

The linear advection equation is then approximated by second-order finite-differences

$$\frac{\psi^{n+1}_{i+1/2} - \psi^n_{i+1/2}}{\tau^{n+1/2}} + \frac{\varphi^{n+1/2}_{i+1} - \varphi^{n+1/2}_i}{h_{i+1/2}} = 0, \tag{2}$$

where the mid-time-layer values are evaluated using trapezoid rule

$$\varphi^{n+1/2}_{i+1} = \tfrac{1}{2}(\varphi^n_{i+1} + \varphi^{n+1}_{i+1}). \tag{3}$$

To complete the system of discretised equations, an upwind second-order extrapolation formula is used

$$\varphi^{n+1}_{i+1} = 2\psi^{n+1/2}_{i+1/2} - \varphi^n_i. \tag{4}$$

The mid-time-level value of the conservative variable $\psi^{n+1/2}_{i+1/2}$ in Eq (4) is obtained at the preceding "predictor" step

$$\frac{\psi^{n+1/2}_{i+1/2} - \psi^n_{i+1/2}}{\frac{1}{2}\tau^{n+1/2}} + \frac{\varphi^n_{i+1} - \varphi^n_i}{h_{i+1/2}} = 0. \tag{5}$$

For the actual implementation, Eqs (2)-(5) are performed in the reverse order, and Eqs (2) and (3) are replaced by a single 'corrector' step (2')

$$\frac{\psi^{n+1}_{i+1/2} - \psi^{n+1/2}_{i+1/2}}{\frac{1}{2}\tau^{n+1/2}} + \frac{\varphi^{n+1}_{i+1} - \varphi^{n+1}_i}{h_{i+1/2}} = 0. \tag{2'}$$

This finite-difference scheme (Eqs (2)-(5)) is explicit and stable under the Courant (CFL) condition $0 \le \tau/h \le 1$. Also, due to the compact computational stencil, the scheme remains second-order accurate on arbitrary spatial and temporal grids, and it requires only one flux residual evaluation $\mathrm{Re}\, s^n_{i+1/2} = \left(\varphi^n_{i+1} - \varphi^n_i\right)/h_{i+1/2}$ per time step.

Another interesting feature of the scheme includes preserving the conservation law for the kinetic energy-like quantity

$$\frac{\partial f}{\partial t} + \frac{\partial f}{\partial x} = 0,\ f = \varphi^2. \tag{6}$$

The additional conservation law is a direct consequence of the original differential equation (Eq (1)). Multiplying Eq (2) by $(\psi_{i+1/2}^{n+1}+\psi_{i+1/2}^{n})/2$ and using Eqs (4),(5) and (2') to re-arrange equations leads to a second-order approximation of the additional conservation law (6)

$$\frac{f_{i+1/2}^{n+1}-f_{i+1/2}^{n}}{\tau^{n+1/2}}+\frac{\left(\varphi_{i+1}^{n+1/2}\right)^2-\left(\varphi_{i}^{n+1/2}\right)^2}{h_{i+1/2}}=0, \qquad (6')$$

where $f_{i+1/2}^{n}$ is a quadratic function, which is positively defined in the CFL stability region $f_{i+1/2}^{n}=\left(\psi_{i+1/2}^{n}\right)^2+\frac{1}{4}\left(h_{i+1/2}\right)^2 CFL\left(1-CFL\right)\left(\frac{\varphi_{i+1}^{n}-\varphi_{i}^{n}}{h_{i+1/2}}\right)^2, CFL=\tau^{n+1/2}/h_{i+1/2}$.

On uniform grids, Eqs (2)-(5) can be re-arranged to exclude the conservative variables in favour of the nodal variable to obtain a non-staggered scheme. The result is a three time-level finite-difference scheme

$$\frac{1}{2}\left[\frac{\varphi_{i+1}^{n+1}-\varphi_{i+1}^{n}}{\tau}+\frac{\varphi_{i}^{n}-\varphi_{i}^{n-1}}{\tau}\right]+\frac{\varphi_{i+1}^{n}-\varphi_{i}^{n}}{h}=0 \qquad (7)$$

which is known as the second-order upwind leapfrog [2,3] or Compact Accurate Boundary-Adjustable high-Resolution (CABARET) scheme [4,5,6,7].

The non-staggered form is well suited to analyse linear wave dissipation and dispersion properties. For example, a travelling wave solution $\varphi_m^n \sim \exp[i\omega\cdot\tau\cdot n - ik\cdot h\cdot m]$ can be substituted in (7) to solve the resulting algebraic equation for the frequency $\omega=\omega(k\cdot h)$. One can then determine the dissipation $\Im m(\omega(k\cdot h)\cdot\tau)\neq 0$ and the dispersion $\omega(k\cdot h)\cdot\tau - k\cdot h\neq 0$ errors as a function of different wave and Courant numbers, $k\cdot h$ and τ/h. In particular, the analysis shows that the CABARET scheme is non-dissipative $\Im m(\omega(k\cdot h)\cdot\tau)=0$ for all wavenumbers $-\pi<k\cdot h<\pi$. Furthermore, the scheme is exact at three Courant numbers $\tau/h=0,0.5,1$.

In computational aeroacoustics, it is common to compare phase errors of different finite-difference methods on a single plane, ε *vs* N_λ, where ε is the phase error $\varepsilon=(K(k\cdot h)-(k\cdot h))/\pi$, and N_λ is the number of grid points per wave lengths (p.p.w.), which is inversely proportional to the spatial wavenumber, $N_\lambda=2\pi/(k\cdot h)$. Measuring the decrease in numerical error with the increase of the grid resolution N_λ is useful for estimating the efficiency of the scheme [**Ошибка! Источник ссылки не найден.**].

The quantity $K(k\cdot h)$ represents the 'numerical' spatial wavenumber obtained by substituting the spatial part of the travelling wave solution $\exp[ik\cdot h\cdot m]$ into the spatial derivative $\frac{\partial\varphi}{\partial x}$ discretised by finite-differences. Assessing the accuracy of temporal differentiation is usually done separately, and it involves analysing a similar quantity for the time derivative, $\varepsilon_\tau=(W(\omega\cdot\tau)-(\omega\cdot\tau))/\pi$.

For the CABARET scheme, it is the combined effect of the space and time approximation which is important, and it is the full space-time dispersion error

$\varepsilon = abs(\omega(k \cdot h) \cdot \tau - (k \cdot h))/\pi$, which characterizes the dispersion properties of the scheme.

In fig.1, phase errors which correspond to several spatial central finite-difference schemes from [**Ошибка! Источник ссылки не найден.**] are shown against those of the CABARET scheme at several different Courant numbers.

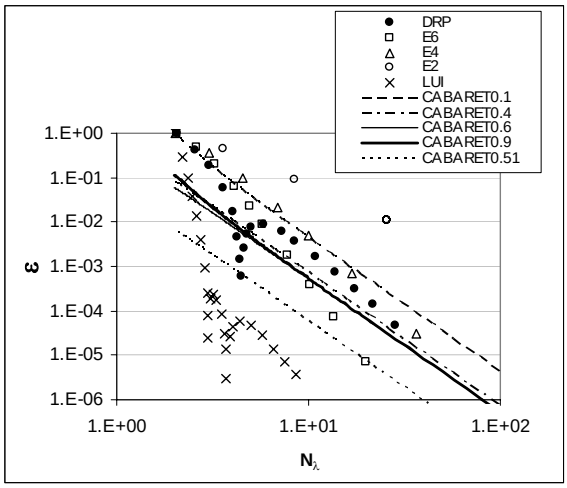

Fig.1: Phase errors of several spatial finite-difference schemes and the CABARET scheme at different CFL numbers. E2, E4, E6 denotes central differences of the second, fourth and sixth-order, DRP denotes the fourth order Dispersion Relation Preserving scheme of Tam and Webb [Ошибка! Источник ссылки не найден.**], LUI stands for the sixth order pentadiagonal compact scheme of Lui and Lele [**Ошибка! Источник ссылки не найден.**], CABARETx stands for the CABARET scheme at a Courant number CFL=x**

It can be seen that even at the least 'optimal' Courant number, CFL=0.1, the error of CABARET scheme remains as low as that of the fourth order central difference scheme for a wide range of p.p.w. parameter N_λ. Furthermore, as it follows from fig.1, in terms of computational efficiency the CABARET scheme compares particularly well to the high-order schemes over a wide range of the phase error, ε. For the spatial finite-difference schemes used together with multi-level Runge-Kutta methods of the same order of accuracy as of the spatial approximation, the computing cost of each scheme may be estimated as the product of the number of points in the spatial stencil at the same time level, the number of p.p.w., $N_\lambda(\varepsilon)$, required, and the number of temporal stages used in each scheme. For accuracy ε=1.e-3, the corresponding costs are summarised in Table I. For the CABARET scheme, the costs are calculated on the basis of a three point stencil, i.e. two nodal values and one centre cell value, which are involved in the calculation at the same time level.

Table I: Computational costs of numerical schemes

Schemes	E4	E6	DRP	DRP (without the dip at N_λ~5)	LUI	CABARETx x=0.1	CABARETx x=0.4,0.6, and 0.9
Number of points per stencil	5	7	7	7	7	3	3
$N_\lambda(\varepsilon)$	20	8	5	20	3	20	9
Cost	400	336	140	420	126	60	27

Another important property pertaining to the linear wave dispersion is the numerical group velocity $c_g = \frac{dK(k \cdot h)}{d(k \cdot h)}$, or $c_g = \frac{d\omega(k \cdot h)}{d(k \cdot h)}$, for the combined spatial and temporal error analysis. Any deviation of the numerical group speed from unity corresponds to incorrect physical wave propagation. In particular, negative values of the numerical group speed lead to the effect of artificial wave reflection from computational grids [**Ошибка! Источник ссылки не найден.**].

In fig.2, the numerical group speeds of different spatial central finite-difference schemes are shown in comparison to those of the CABARET scheme at several different Courant numbers. It can be seen that all but the highest accuracy central schemes have regions of negative group speeds. In contrast, the negative speed regions associated with coarse grid reflection is not a problem for the CABARET scheme; its numerical group speed always remains in the physically correct direction. On coarse grids at the least 'optimal' CFL number, CFL=0.1 the CABARET scheme shows some abnormal linear wave dispersion effects. These errors remain relatively small in the most of the spectra, and they are comparable in magnitude to the group speed errors of the fourth order central differences.

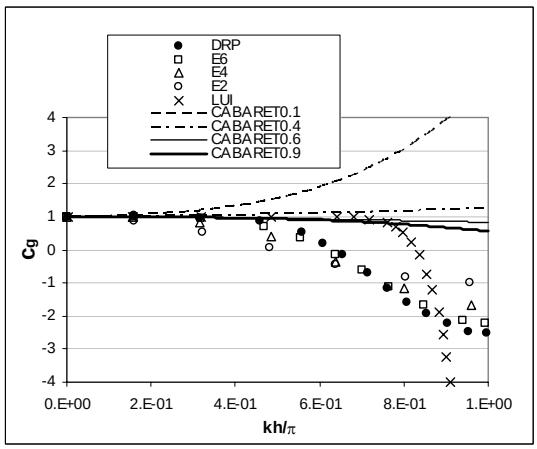

Fig.2 Numerical group speeds of several spatial finite-difference schemes and the CABARET scheme at several different CFL numbers.

1.3. Non-linear correction procedure

As other non-dissipative schemes CABARET needs a mechanism to remove short-wave oscillations which emerge when under-resolved gradients appear in the solution. A fundamental reason for the presence of non-physical oscillations is violation of the maximum principle in the numerical solution. For the scalar advection equation the maximum principle appears as an additional constraint which does not allow to create any new minima or maxima in the solution. In the CABARET method an appropriate non-linear correction method is used to reinforce the maximum principle. In contrast to standard TVD limiting approaches [8] in CABARET a less restrictive procedure is used which employs three stencil points staggered in one cell.

$$\varphi_{i+1}^{n+1} = 2\psi_{i+1/2}^{n+1/2} - \varphi_i^n,$$
$$Max = \max(\varphi_i^n, \varphi_{i+1}^n, \psi_{i+1/2}^n), \qquad Min = \min(\varphi_i^n, \varphi_{i+1}^n, \psi_{i+1/2}^n),$$
$$If \;\; \varphi_{i+1}^{n+1} > Max, \quad \varphi_{i+1}^{n+1} = Max,$$
$$If \;\; \varphi_{i+1}^{n+1} < Min, \quad \varphi_{i+1}^{n+1} = Min.$$

1.4. Extension to the non-linear Euler equations

The extension of the CABARET scheme to the nonlinear Euler equations is obtained by introducing the dual variables of conservative-type and advection-type to describe the compressible flow both in conservation and primary form.

For example, the 2-D non-linear Euler conservation form is given by

$$\frac{\partial \mathbf{U}}{\partial t} + \frac{\partial \mathbf{F}}{\partial x} + \frac{\partial \mathbf{G}}{\partial y} = 0;$$
$$\mathbf{U}^T = (\rho, \rho u, \rho v, \rho E); \mathbf{F}^T = (\rho u, \rho u^2 + p, \rho uv, \rho uE + up);$$
$$\mathbf{G}^T = (\rho v, \rho uv, \rho v^2 + p, \rho vE + vp); E = \varepsilon + \left(u^2 + v^2\right)/2; p = (\gamma - 1) \cdot \rho \cdot \varepsilon;$$

and the primary form is equivalent to quasi-linear representation of the same equations

$$\frac{\partial \mathbf{V}}{\partial t} + \mathbf{A}\frac{\partial \mathbf{V}}{\partial x} + \mathbf{B}\frac{\partial \mathbf{V}}{\partial y} = 0;$$
$$\mathbf{V}^T = (\rho, u, v, p)$$

were standard notations [9] are used for the vector of conservative variables and fluxes, **U, F** and **G,** and matrices of primary variables **A** and **B,** where ρ is density, u and v are Cartesian velocity components, p is pressure, and ε and E are internal and total energy, respectively.

The equations in primary variables can be further re-arranged into a characteristic form by using a linear change of variables to diagonalize the matrix $\mathbf{A}k_x + \mathbf{B}k_y$ where $\mathbf{k} = (k_x, k_y)$ is an arbitrary unit vector.

In multiple dimensions, the characteristic direction may be chosen to align with one of the coordinate directions, x and y

$$\begin{aligned} &\frac{\partial \mathbf{R_x}}{\partial t} + \mathbf{\Lambda_x} \cdot \frac{\partial \mathbf{R_x}}{\partial x} = \mathbf{g_x}; \delta \mathbf{R_x} = \mathbf{L_x} \cdot \delta \mathbf{V}; \\ &\frac{\partial \mathbf{R_y}}{\partial t} + \mathbf{\Lambda_y} \cdot \frac{\partial \mathbf{R_y}}{\partial y} = \mathbf{g_y}; \delta \mathbf{R_y} = \mathbf{L_y} \cdot \delta \mathbf{V} \end{aligned} \tag{8}$$

where $\mathbf{L_x}$ and $\mathbf{L_y}$ are the left eigen-matrices in the x and y-direction, and $\mathbf{R_x}$ and $\mathbf{R_y}$ are the vectors of Riemann local -invariants. The source terms appearing on the right hand side are due to the partial derivatives in the tangential direction, $\mathbf{g_x} = -\mathbf{L_x} \cdot \mathbf{B} \cdot \frac{\partial \mathbf{V}}{\partial y}$, $\mathbf{g_y} = -\mathbf{L_y} \cdot \mathbf{A} \cdot \frac{\partial \mathbf{V}}{\partial x}$. For non-homogeneous Euler or Navier Stokes equations, the right hand side source terms will also include the terms arising from physical sources and/or viscous fluxes.

Similar to the scalar advection equation, the maximum principle can be introduced for the system of Euler equations in the characteristic form as an additional constraint to the governing equations. For example, in the x-direction, the invariants are to be limited by

$$\left(\mathbf{R}_x\right)^{\min} < \mathbf{R}_x^{\,t=t_0+\tau} < \left(\mathbf{R}_x\right)^{\max};\left(\mathbf{R}_x\right)^{\min/\max} = \max/\min\left(\mathbf{R}_x\right)_{t=t_0} + \int_{t_0}^{t_0+\tau} \mathbf{g}_x dt\,.$$

Details of the numerical procedure for the gas dynamics equations can be found in [6]. In the numerical examples to follow the properties of the CABARET scheme pertinent for inviscid compressible flows will be demonstrated. The solution of the CABARET scheme in all cases will be represented by conservative-type centre cell variables.

2. NUMERICAL EXAMPLES

2.1. 1-D Linear advection test

It is first instructive to compare the CABARET scheme against other second-order schemes which also use non-linear procedures to reinforce the maximum principle in the solution. Fig.3 shows results of the linear advection of a rectangular pulse and a half-period sine wave for a one-stage second-order Van Leer TVD scheme, with MinMod and Superbee limiters, and the CABARET scheme with the nonlinear correction. These non-linear TVD schemes are as CPU expensive as the CABARET scheme. The computations are performed on the same periodic grid and at the same Courant number. We observed that the CABARET scheme preserves the discontinuous profile well, and it does not lead to any artificial "staircasing" of the smooth profile typical of some TVD schemes at higher Courant numbers.

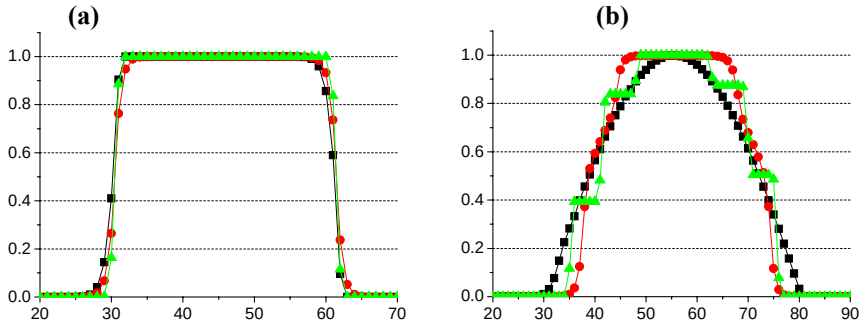

Fig.3 Profiles of (a) – a rectangle and (b) – a half-period sine wave in 1-D linear advection tests after 250 time steps on a uniform spatial grid with h = 1 at CFL = 0.45; squares denote the solution of the CABARET scheme, circles and triangles denote the solution of a second-order Van Leer scheme with TVD MinMod limiter and TVD Superbee limiter, respectively

2.2. 1-D Shock-tube problem

To illustrate the shock-capturing capability of the CABARET scheme, the 1-D shock-tube problems from [10] is considered. In comparison to a standard "Sod tests" [9] the perfect gas has a higher density as well as a higher pressure ratio across the initial discontinuity:

$$\text{Problem 1: } (\rho,u,p) = \begin{cases} (1000,0,1000) & \text{if } 0 \le x < 0.3 \\ (1,0,1) & \text{if } 0.3 < x \le 1 \end{cases}$$

$$\text{Problem 2: } (\rho,u,p) = \begin{cases} (10000,0,10000) & \text{if } 0 \le x < 0.3 \\ (1,0,1) & \text{if } 0.3 < x \le 1 \end{cases}$$

Fig.4 shows computed density and velocity solution at a control time t=0.15 for the first order Godunov scheme from [10] and the CABARET scheme in comparison to the analytical solution. In comparison to the first-order scheme, the CABARET solution is much less smeared by numerical viscosity.

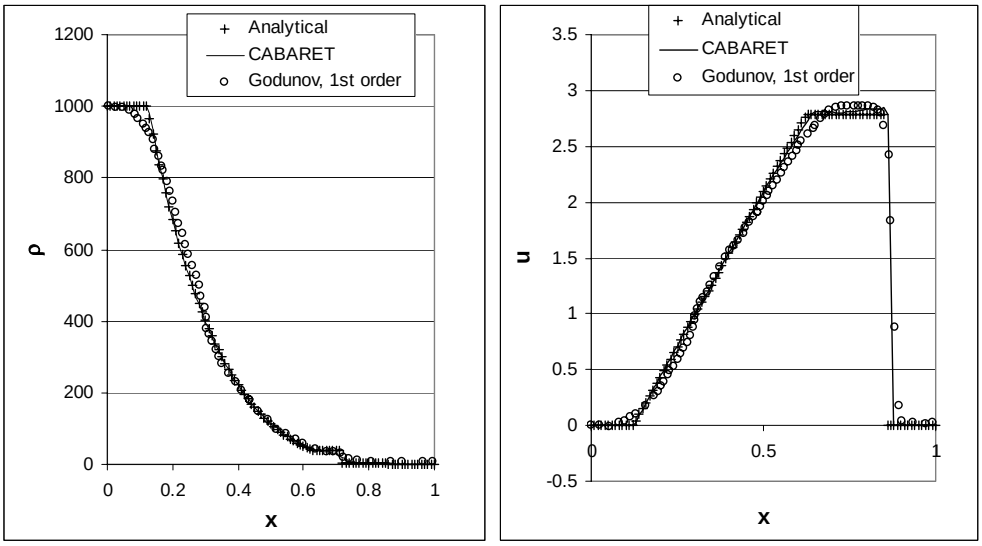

(a) **(b)**

Fig.4 Solutions of Problem 1 at a control time t=0.15 of the CABARET scheme, a first-order Godunov scheme [10], and the analytical solution, (a) – density and (b) – velocity

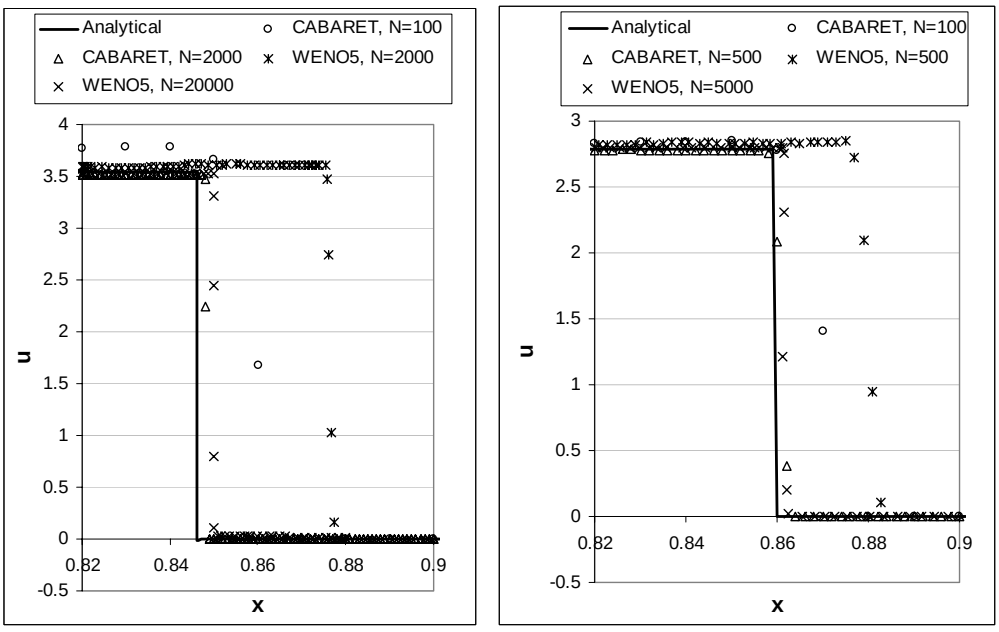

(a) **(b)**

Fig.5 A close-up view for the velocity profile across the shock: comparing the CABARET solution with the fifth-order WENO scheme (WENO5) [10], (a) – Problem 1, t=0.15 and (b) – Problem 2, t=0.12

In contrast to popular high-resolution long-stencil schemes, such as a Roe scheme with the Van Leer Method for Upwind Scalar Conservation Laws (MUSCL), a Discontinuous Galerkin (DG) scheme, and a Weighted Essentially Non-Oscillatory (WENO) scheme, which have a very slow convergence of the velocity across the shock [10], the CABARET scheme remains accurate. Fig.5 shows that in comparison with the fifth-order WENO scheme the CABARET scheme is accurate on grids which are in order of magnitude coarser.

2.3. 2-D linear advection of an isentropic vortex

The next example shows the capability of the scheme to accurately resolve vortical disturbances in a uniform flow at an angle to the computational grid. In the test [11], an isentropic vortex is introduced to a uniform mean flow at 45^0 to the grid lines, by perturbations in the density, velocity and pressure. The background flow and the perturbation parameters are given, respectively, by

$$(\rho_\infty, u_\infty, v_\infty, p_\infty) = (1,1,1,1)$$

and

$$\rho' = \rho_\infty \left[\left(1 - \frac{(\gamma-1)\alpha^2}{8\pi^2\gamma} \exp\left\{1-(x-x_0)^2-(y-y_0)^2\right\} \right)^{1/(\gamma-1)} - 1 \right];$$

$$u' = -(y-y_0)\frac{\alpha}{2\pi}\exp\left\{0.5\left[1-(x-x_0)^2-(y-y_0)^2\right]\right\};$$

$$v' = (x-x_0)\frac{\alpha}{2\pi}\exp\left\{0.5\left[1-(x-x_0)^2-(y-y_0)^2\right]\right\};$$

$$p' = p_\infty \left[\left(1 - \frac{(\gamma-1)\alpha^2}{8\pi^2\gamma} \exp\left\{1-(x-x_0)^2-(y-y_0)^2\right\} \right)^{\gamma/(\gamma-1)} - 1 \right];$$

$$\alpha = 5$$

As in [11], the problem is solved in a periodic domain [0,10]x[0,10] on a set of grids 40 by 40, 80 by 80 and 160 by 160, which correspond to grid refinement parameters n=1, 4 and 16. Similar to [11], the numerical error is based on density and defined in a standard way

$$L_1 = \frac{1}{(N+1)^2}\sum_{i=0}^{N}\sum_{j=0}^{N}\left|\rho_{i,j} - \rho_{i,j}^{exact}\right|.$$

In Table II, the errors of several finite-difference schemes from [0] and the CABARET scheme are shown for a control time moment t=2. For each scheme, the number of operations per time step (the cost) is evaluated as a product of the grid refinement parameter, the number of points in the spatial stencil, and the number of temporal stages.

Table II: Numerical errors and costs for the 2-D vortex advection problem

N		CABARET	C4	WENO	ENO^A	MUSCL^A	WENO^A

1	Error Cost	6.9e-4 5	1.1e-3 40	9.3e-4 70	7.8e-4 30	1.2e-3 30	6.1e-4 70
4	Error Cost	1.8e-4 20	**5.7e-5** **160**	**7.0e-5** **280**	**6.6e-5** **120**	**2.7e-4** **120**	**4.5e-5** **280**
16	Error Cost	**5.0e-5** **80**	3.7e-6 640	2.4e-6 1120	7.8e-6 480	5.3e-5 480	2.9e-6 1120

Legend: C4 is the fourth order accurate, conservative centred scheme; Essentially non-oscillatory scheme (ENO) is of the third order; Van Leer variable extrapolation scheme (MUSCL) is of the third order; Weighted essentially non-oscillatory scheme (WENO) is of the fifth order; ^{A} denotes that the C4 scheme is used as the basic scheme.

Fig.6 shows instantaneous density profiles in the vortex cross-section at y=5, and the reference analytical solution for two later time moments, t=10 and t=100, on a grid of 100 by 100 cells. It can be seen that both the phase and the amplitude of the vortex are well preserved during its advection over long distances.

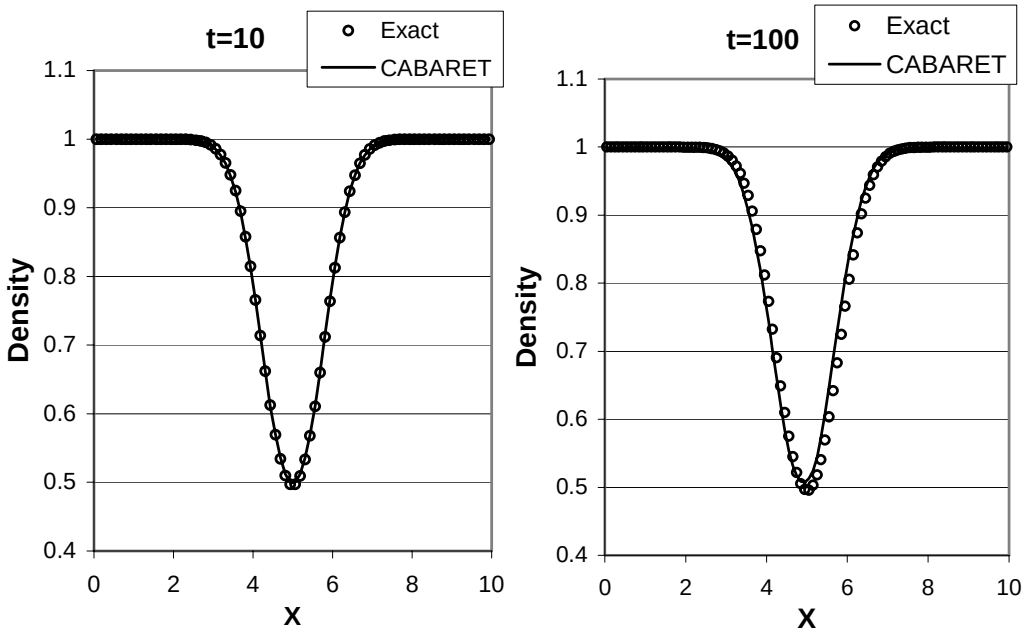

Fig.6 Instantaneous density profiles in the central cross section plane at two time moments for the problem of 2D isentropic vortex advection in a uniform mean flow

2.4. Double Mach reflection

In a square computational domain $[0,4]\times[0,1]$ the reflective wall lies on the bottom starting from x=1/6. At initial time the right moving Mach 10 shock, which makes an angle of 60^0 with the x-axis, crosses the bottom boundary at x=1/6. The benchmark problem is solved on three uniform grids 480 by 120 cells, 960 by 240 cells and 1920 by 480 cells. Fig.7 shows a close-up of computed density fields at a typical control time.

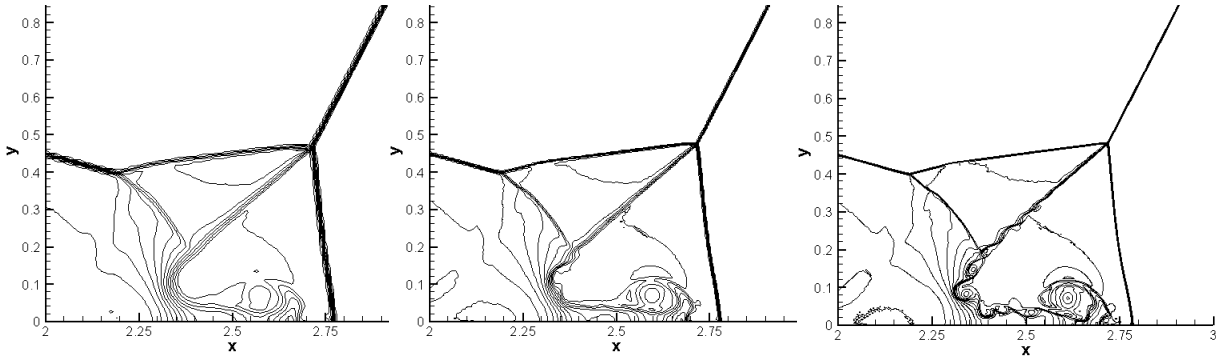

Fig. 7 Density fields for the double Mach reflection problem; computational grids (a) 480 by 120 cells, (b) 960 by 240 cells and (c) 1920 by 480; 30 density contours are plotted from 1 to 22

It can be seen that as the grid becomes more refined the finer flow structure with small eddies in the vicinity of the λ-shock becomes more visible. These vortices grow with time and may be attributed to the development of the Kelvin-Helmholz instability which occurs in inviscid flows with shear gradients. The fact that these are not suppressed by numerical viscosity indicates that the overall scheme has indeed a very low numerical dissipation. The fine flow-field structure observed is in a good agreement with computational predictions of more CPU intensive, high-order Arbitrary Derivative (ADER) and Discontinuous Galerkin-Weighted essentially non-oscillatory (DG-WENO) methods reported for the same grids in the literature [12,13].

2.5. Propagation of an acoustic Gaussian pulse on a non-uniform grid

To test the capability of the CABARET scheme to accurately resolve and transmit acoustically small fluctuations on non-smooth computational grids in open domains, the evolution of initial pressure disturbance in a free space is considered.

At the initial time moment, an isentropic Gaussian pressure pulse $p' = \varepsilon \cdot \exp(-\beta \cdot \left[(x-x_0)^2 + (y-y_0)^2 \right]); \beta = 0.4\ln(2)$ is specified in the centre of a computational domain $(-3 \le x \le 3; -3 \le y \le 3)$, with open boundaries, as a perturbation to uniform flow field, $\rho_\infty = 1; u_\infty = 0; v_\infty = 0; p_\infty = 1/\gamma$, where ε=1.e-5.

In the test, the problem is computed in a half computational domain $-3 \le x \le 3; 0 \le y \le 3$ with a symmetry condition at the bottom boundary, *y*=0. A uniform Cartesian grid is used in the left part of the domain $(-1 \le x \le 3, 0 \le y \le 3)$, of 73 by 50 cells, and a stretched uniform grid, which is obtained by stretching the original grid in three times in the axial direction, is used in the remaining part of the domain $(-3 \le x < -1, 0 \le y \le 3)$, of 9 by 50 cells, respectively. Across x= -1, the grid cell size distribution thus has a discontinuity.

Instantaneous pressure perturbations normalised by the amplitude of the initial pulse, $p'\varepsilon^{-1} = \varepsilon^{-1}(p - p_\infty)/p_\infty$ are shown in fig.8a,b. In the snapshots, a Gaussian-type pulse in pressure, which corresponds to the original pressure fluctuation, is shown to propagate through the computational domain without a noticeable attenuation of amplitude, or loss of the symmetry of the solution profile despite the pulse propagation through the discontinuous fine/coarse grid interface. We emphasize that there was no

special treatment introduced in the CABARET scheme to deal with this grid singularity. The fact that the scheme appears to be not sensitive to the grid non-smoothness follows from the extremely tight computational stencil of the scheme and the absence of negative, non-physical group wave speeds at higher wavenumbers, as it was shown in fig.2.

Fig. 8c shows pressure time signals obtained for two control points, A and B, which are positioned at the same distance R=2 from the centre of the pulse at 90^0 and 180^0 to the x-axis. It was confirmed by a further grid refinement study that the solution obtained at point A is converged within less than one percent error in amplitude of the pressure peak and, therefore, will be further used as a reference solution. In comparison to the reference solution, in the coarse region of the grid, at point B, the acoustic wave amplitude is reasonably well preserved (within 10-12%) and, again, shows no sign of spurious grid reflections.

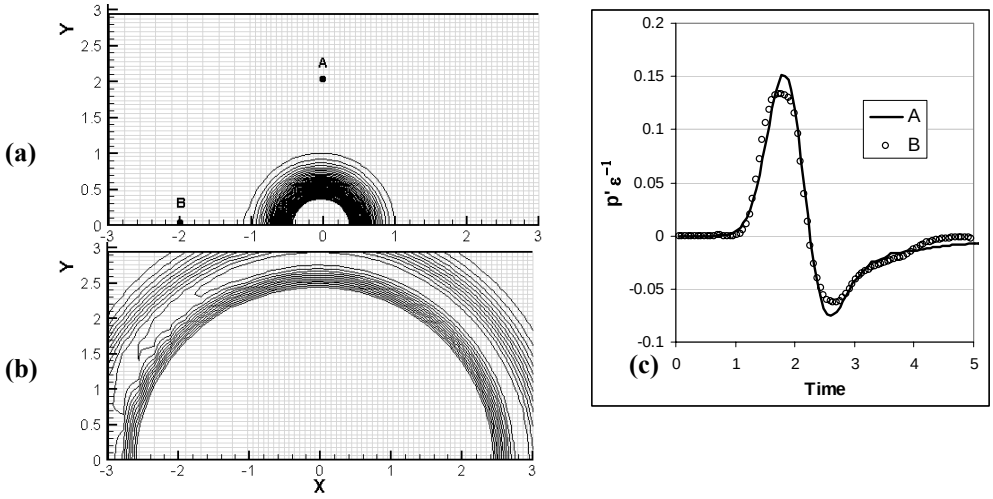

Fig.8 Computed pressure perturbation fields at two time moments, t=0 – (a) and t=2.4 – (b) for the 2-D Gaussian acoustic pulse evolving in an open-domain free-space field (50 contour lines of positive pressure perturbations are shown), and the time signals obtained in points A and B (shown in fig.8a) of the computational domain

2.6. 2-D Acoustic wave diffraction from a cylinder

The next test example involves computation on a curvilinear grid and is a benchmark problem from the second Computational aeroacoustics workshop. At initial time moment an acoustic perturbation is specified four diameters downstream from a 2-D-cylinder with no mean flow. There is a primary propagating acoustic wave and a secondary one, reflected from the cylinder boundary. The pressure signal is computed at three reference points A, B and C around the cylinder and compared against the analytical solution, which was obtained as a Bessel function series.

The full non-linear Euler equations are solved with the CABARET scheme in a computational domain with a symmetry condition on the bottom boundary on two curvilinear H-type Cartesian grids of 200 by 100 and 400 by 200 cells (fig.9). The results are in a good agreement with the analytical solution (fig.10), and are no less accurate than those obtained on similar grids by solving a simpler, linearised system of Euler equations, as reported in the literature [14].

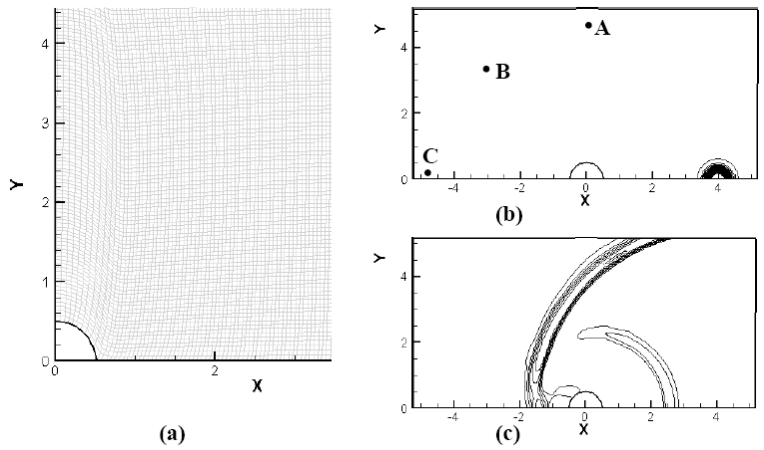

Fig. 9 Computational grid in the vicinity of the cylinder– (a) and contour lines of instantaneous pressure fluctuations at t=0 – (b) (with a schematic of control points A,B and C shown), and t=6 – (c), grid 200 by 100 cells.

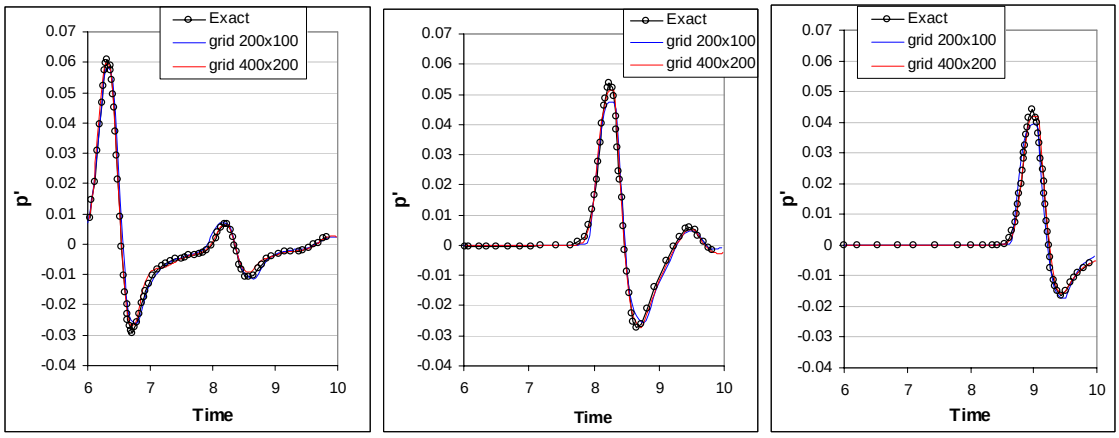

Fig. 10 Comparison with the analytical solution, pressure fluctuations at control points: A – (a), B – (b), and C – (c)

2.7. A 2-D steady inviscid compressible flow around a zero-incidence NACA0012 in a high-subsonic wind tunnel

Finally, our last example is concerned with a steady compressible flow in a curvilinear grid domain. Unlike potential flow methods, which are only applicable for relatively low-Mach number flows, a spurious numerical entropy generation is a typical problem when solving the Euler equations numerically around a curvilinear boundary [15].

In inviscid flow computations, the extra dissipation is generated when the solution meets a discontinuity introduced to the flow by the solid boundary. For less smooth profiles, the spurious entropy generation leads to a bigger numerical boundary layer developed. The numerical boundary layer has a qualitatively similar behaviour to the physical boundary layer and manifests itself in a shear-flow-like gradient close to the boundary. Unlike the physical boundary layer, however, the generation of numerical boundary layer is of course totally spurious, and should be avoided.

For a flow around a typical airfoil, which rapidly decelerates in the vicinity of the leading edge, standard dissipative numerical schemes generate a noticeable numerical

boundary layer which can only be reduced by a significant grid refinement. The grid refinement in this case is more of a "cosmetic" fix since it is not dictated by the physics of the inviscid compressible flow.

To illustrate the point we consider a steady compressible flow around a NACA00012 profile in a wind tunnel. The steady problem is to be solved with an unsteady numerical Eularian method and with no special treatment of the airfoil boundary to obscure the effect of numerical entropy generation. The computational domain is $0<x<3$, $0<y<0.75$ and the airfoil chord length is 1. A structured H-grid, which is uniform in the y-direction, will be used to manifest any spurious entropy generation.

Fig.11a,b show the Mach number contours for a transonic test problem which corresponds to the free-stream $M_\infty=0.7$, as computed with the CABARET scheme on two grids, 200 by 50 and 400 by 100 cells. The solution is well converged, and the weak shock wave, which appears on the airfoil boundary, is well resolved without spurious oscillations, within two-three computational cells on the curvilinear grid. We also notice that the Mach number contours lie almost perpendicular to the airfoil boundary; their deviation from normal is localized within the last grid cell in the normal direction.

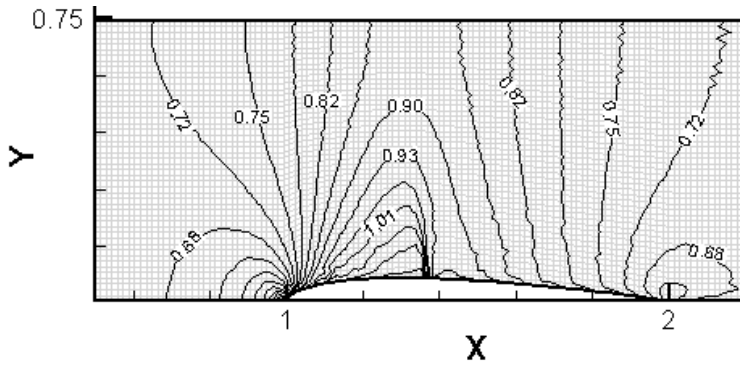

(a)

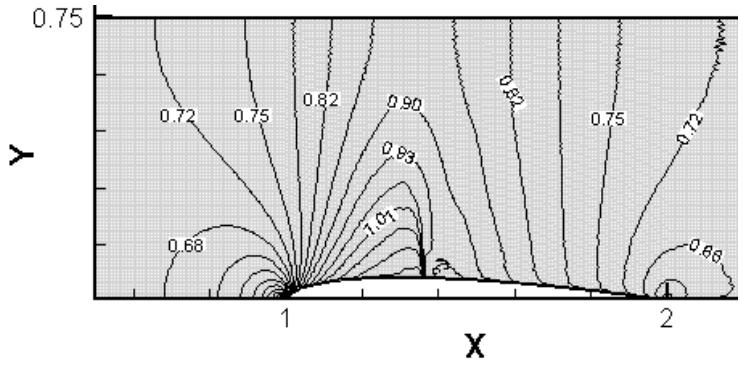

(b)

Fig. 11 Mach contour lines for the steady flow calculation of the CABARET scheme around NACA0012 in a wind tunnel at $M_\infty=0.7$, (a) - grid 200 by 50 cells, (b) – grid 400 by 100 cells

For the same problem at a lower free-stream Mach number, $M_\infty=0.5$, which is sufficiently away from the wind-tunnel chocking condition, the convergence of the CABARET scheme (fig.12) has been compared with an "industry-standard" shock-capturing method, based on a third-order characteristic Roe scheme with MUSCL TVD MinMod limiting (fig.13).

Computations have been performed on similar H-type numerical grids: 100 by 25, 200 by 50 and 400 by 100 cells.

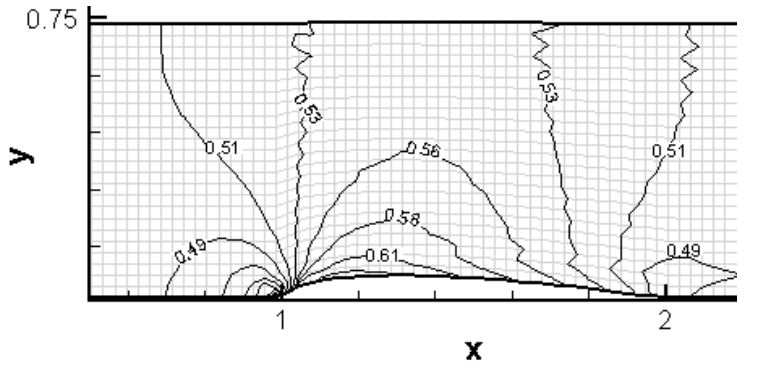

(a)

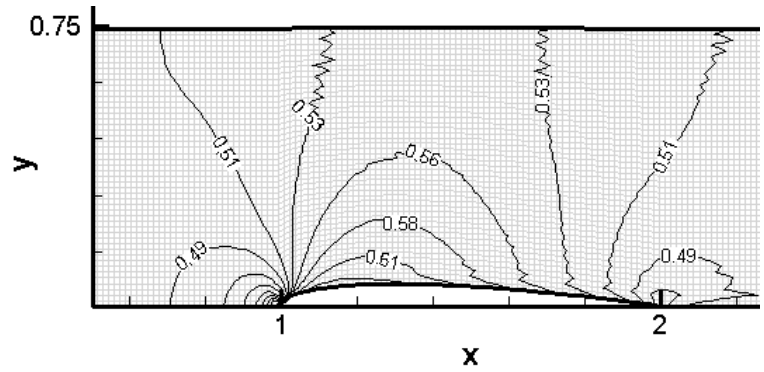

(b)

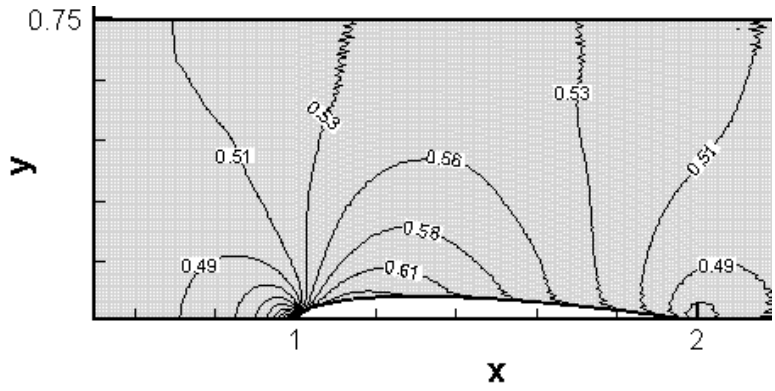

(c)

Fig. 12 Mach contour lines for the steady flow calculation of the CABARET scheme around NACA0012 in a wind tunnel at M_∞=0.5, (a) grid 100 by 25 cells, (b) grid 200 by 50 cells, (c) grid 400 by 100 cells

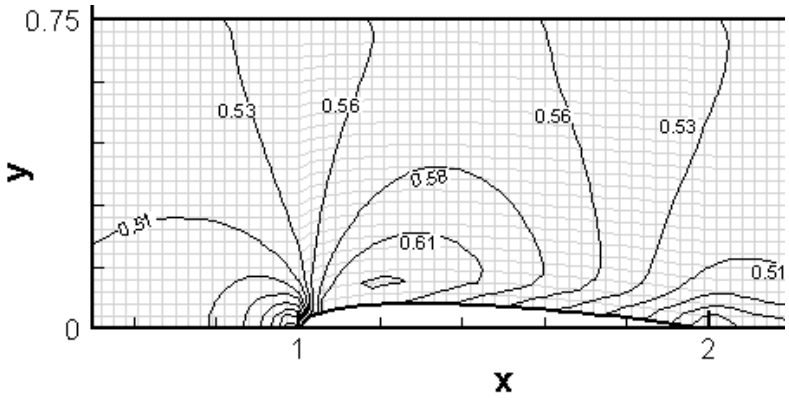

(a)

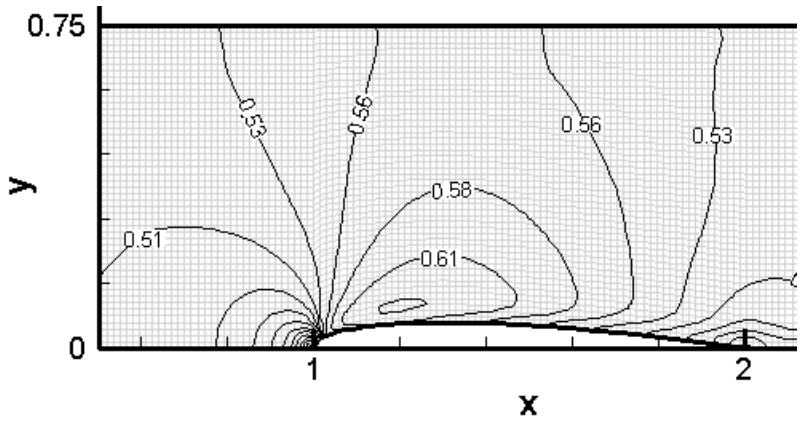

(b)

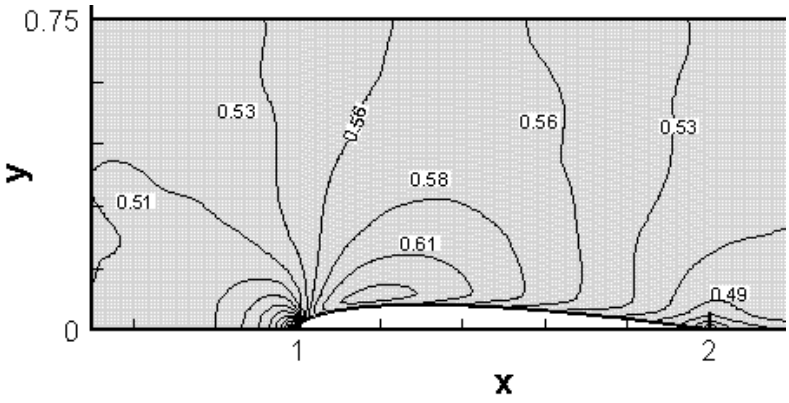

(c)

Fig. 13 Mach contour lines for the steady flow calculation of a third-order Roe-MUSCL-TVD method around NACA0012 in a wind tunnel at M_∞=0.5, (a) grid 100 by 25 cells, (b) grid 200 by 50 cells, (c) grid 400 by 100 cells

It can be seen that the CABARET scheme produces a much better converged solution in comparison to the Roe MUSCL TVD scheme. The latter is more numerically dissipative and produces a more "viscous" solution of the inviscid problem even on the finest grid. The bigger numerical dissipation of the Roe MUSCL TVD scheme leads to a thicker

numerical boundary layer, which is spread across 4-5 grid cells. For the CABARET scheme, the region of spurious shear velocity gradient close to the boundary is limited to just 1 cell. We also note that in contrast to the Roe MUSCL TVD scheme the solution of the CABARET scheme has some minor short-wave oscillations, which are non-suppressed by the numerical viscosity, and which are typical of other low-dissipative numerical schemes. These minor oscillations could be reduced by a post-processing filtering applied to the present solution, which is based on the conservative-type variables. For example, the flow solution could be represented by a local cell average of the four advection-type and one conservative-type variables which are available in each cell.

3. CONCLUSIONS

A new efficient numerical method is proposed for linear and non-linear inviscid compressible flow problems.

The new method combines the simplicity and robustness of shock-capturing finite-volume approaches and the physical insight of the method of characteristics. At the same time, the method remains suitable at linear flow regimes where preserving linear wave non-dissipative and dispersion is essential.

For a range of test problems, it was shown that the new method remains very robust and computationally more efficient than several popular high-resolution schemes. The extension of the method to more complicated geometries and viscous flows will be the subject of future work.

4. ACKNOWLEDGEMENT

The support by the Royal Society of London is gratefully acknowledged. Work was supported by the Russian Foundation for Basic Research.

5. REFERENCES

[1] Colonius T, Lele SK. Computational aeroacoustics: progress on nonlinear problems of sound generation. Progress in Aerospace sciences, 2004, **40**: 345-416.

[2] Iserles, A., Generalized Leapfrog Methods, IMA Journal of Numerical Analysis, 6 (1986), No 4, 381-392.

[3] Thomas, J.P. and Roe, P.L., Development of Non-Dissipative Numerical Schemes for Computational Aeroacoustics, AIAA Paper 93-3382.

[4] Goloviznin, V.M. and Samarskii, A.A., Difference approximation of convective transport with spatial splitting of time derivative, Mathematical Modelling, 10(1998)**,** No 1, 86-100.

[5] Goloviznin, V. M., Balanced Characteristic Method for Systems of Hyperbolic Conservation Laws, Doklady Mathematics, Vol. 72, No. 1, July-August 2005, 619-623.

[6] Karabasov SA, Goloviznin VM, Kozubskaya TK and Abalakin IA. A New High-Resolution Balance-Characteristic Method for Aeroacoustics, AIAA-2006-2415

paper, 12th AIAA/CEAS Aeroacoustics Conference (27th AIAA Aeroacoustics Conference), Cambridge, Massachusetts, May 8-10, 2006.

[7] Karabasov SA and Goloviznin VM. A new efficient high-resolution method for nonlinear aeroacoustics problems, AIAA Journal, in press

[8] Harten, A., Engqist, B., Osher, S., and Chakravarthy, S. Uniformly High Order Accurate Essentially Non-Oscillatory Schemes III, *J. Comput. Phys*, 71, No 2, 1987, 231-303

[9] Hirsch C Numerical computation of internal and external flows, Fundamentals of Computational Fluid Dynamics, Second Edition, J.Wiley & Sons, Ltd, 2007.

[10] Tang H and Liu T. A note on the conservative schemes for the Euler equations. Journal of Computational Physics, 218(2006), 451-459.

[11] Zhou, Y.C. and Wei G.W., High-resolution conjugate filters for the simulation of flows, J. Comp. Phys, 189, No 1, 2003, 159-179.

[12] Titarev, V.A. and Toro E.F., ADER: Arbitrary high order Godunov approach, J. Sci. Comput., 17, Nos 1-4, 2002, 609-618.

[13] Qiu, J. and Shu, C.W., Runge-Kutta Discontinuous Galerkin Method Using WENO Limiters, SIAM Journ. of Scientific Comput., 26, N 3, 2005, 907-929.

[14] Tam CKW and Hardin JC (editors), NASA Technical report CP3352, June 1997.